

Stellar halo substructure generated by bar resonances

Adam M. Dillamore,¹* Vasily Belokurov,¹ N. Wyn Evans¹ and Elliot Y. Davies¹

¹*Institute of Astronomy, University of Cambridge, Madingley Road, Cambridge CB3 0HA, UK*

Accepted XXX. Received YYY; in original form ZZZ

ABSTRACT

Using data from the *Gaia* satellite’s Radial Velocity Spectrometer Data Release 3 (RVS, DR3), we find a new and robust feature in the phase space distribution of halo stars. It is a prominent ridge at constant energy and with angular momentum $L_z > 0$. We run test particle simulations of a stellar halo-like distribution of particles in a realistic Milky Way potential with a rotating bar. We observe similar structures generated in the simulations from the trapping of particles in resonances with the bar, particularly at the corotation resonance. Many of the orbits trapped at the resonances are halo-like, with large vertical excursions from the disc. The location of the observed structure in energy space is consistent with a bar pattern speed in the range $\Omega_b \approx 35 - 40 \text{ km s}^{-1} \text{ kpc}^{-1}$. Overall, the effect of the resonances is to give the inner stellar halo a mild, net spin in the direction of the bar’s rotation. As the distribution of the angular momentum becomes asymmetric, a population of stars with positive mean L_z and low vertical action is created. The variation of the average rotational velocity of the simulated stellar halo with radius is similar to the behaviour of metal-poor stars in data from the APOGEE survey. Though the effects of bar resonances have long been known in the Galactic disc, this is strong evidence that the bar can drive changes even in the diffuse and extended stellar halo through its resonances.

Key words: Galaxy: kinematics and dynamics – Galaxy: halo – Galaxy: structure

1 INTRODUCTION

The first person to entertain the idea that the Milky Way is a barred galaxy seems to have been [de Vaucouleurs \(1964\)](#), based on kinematic evidence of deviations from circular motions in the 21-cm line profiles near the Galactic centre. Curiously, though, [de Vaucouleurs \(1964\)](#) has the orientation of the bar wrong, with the near side at negative Galactic longitudes, rather than positive. The first clear evidence that the Milky Way is barred with the near side at positive longitudes seems to have come from infrared photometry. Both integrated 2.4 μm emission ([Blitz & Spergel 1991](#)) and the distribution of IRAS Miras ([Whitlock 1992](#)) clearly showed the inner Galaxy is brighter at positive longitudes. Work on the gas kinematics ([Binney et al. 1991](#)), the starcounts of red clump giants ([Stanek et al. 1994](#)) and especially the infrared photometric maps obtained by the COBE satellite ([Weiland et al. 1994](#)) added to the growing evidence of a barred Milky Way, which became a consensus by the mid 1990s.

Many of the parameters of the bar in the Milky Way have been constrained in recent years. The pattern speed of the bar Ω_b controls its length. The stellar orbits that support the bar cannot exist much beyond corotation ([Contopoulos 1980](#)). Older studies matching the gas flows suggested a fast and short bar with Ω_b in the range 50 to 60 $\text{kms}^{-1} \text{ kpc}^{-1}$ ([Fux 1999](#); [Bissantz et al. 2003](#)). As the quality and quantity of the gas data has improved, more recent works have determined lower values, consistent with a slower and longer bar ([Sormani et al. 2015](#); [Li et al. 2022](#)). The pattern speed of the bar is now thought to lie in the range 35 to 40 $\text{kms}^{-1} \text{ kpc}^{-1}$ (e.g. [Portail et al. 2017](#); [Wang et al. 2013](#); [Sanders et al. 2019](#); [Binney 2020](#);

[Chiba & Schönrich 2021](#)). This is consistent with results from stellar kinematics – for example, use of the projected continuity equation or [Tremaine & Weinberg \(1984\)](#) method by [Sanders et al. \(2019\)](#), or modelling of multiple bulge stellar populations using spectroscopic data ([Portail et al. 2017](#)).

The bar angle – that is the angle between the line joining the Sun and Galactic Centre and the major axis of the bar – is more uncertain. Studies reaching to longitudes $|\ell| > 10^\circ$ often find bar angles $\approx 45^\circ$ (e.g., [González-Fernández et al. 2012](#)). In studies confined to the inner parts, bar angles of 20° – 35° are typical (e.g., [Stanek et al. 1997](#); [Wegg et al. 2015](#); [Simion et al. 2017](#)). It has been suggested that the Galaxy contains two bars, with the central bar not aligned with the long bar (e.g. [Hammersley et al. 2000](#); [Benjamin et al. 2005](#); [Cabrera-Lavers et al. 2007, 2008](#); [Churchwell et al. 2009](#)). Such a configuration is however difficult to explain dynamically, and it has been shown that these observations can be reproduced with a single structure made up of a boxy bulge and long bar ([Martinez-Valpuesta & Gerhard 2011](#)).

Resonant perturbation theory ([Lynden-Bell & Kalnajs 1972](#); [Lynden-Bell 1973](#)) was introduced into galactic dynamics to understand the trapping of stellar orbits by bar-like perturbations. For nearly circular orbits in a disc, the effects of the bar are most significant at the corotation and Lindblad resonances (e.g., [Shu 1991](#)). [Kalnajs \(1991\)](#) first suggested that this effect may be responsible for creation of the Hyades and Sirius streams in the disc. The closed orbits inside and outside the outer Lindblad Resonance are elongated perpendicular and parallel to the bar in this picture. Subsequently, [Dehnen \(1998\)](#) used *HIPPARCOS* data to demonstrate the existence of abundant substructure or moving groups in the disc, which he ascribed partly to resonance effects. The *Gaia* data releases have

* E-mail: amd206@cam.ac.uk (AMD)

revealed abundant ridges, undulations and streams in velocity or action space, sculpted by the Galactic bar (e.g., [Fragkoudi et al. 2019](#); [Khoperskov et al. 2020](#); [Trick et al. 2021](#); [Trick 2022](#); [Wheeler et al. 2022](#)).

The idea that the Galactic bar can create substructure in the disc is well-established. The disc orbits are nearly circular and confined largely to the Galactic plane, so it is easy to see how a rotating bisymmetric disturbance can couple to the orbits. By contrast, in the halo, stars are moving on eccentric orbits and can reach heights of many kiloparsecs above the Galactic plane. While less well studied, numerical experiments suggest that these stellar orbits may still be susceptible to trapping by bar resonances ([Moreno et al. 2015a](#)). In addition, the effects of bars on the dark halo has been the subject of much debate over the last decades (e.g., [Ceverino & Klypin 2007](#); [Debattista & Sellwood 1998, 2000a](#); [Weinberg & Katz 2002](#)). The slowing of bars by dynamical friction of the dark matter halo can change the central parts from cusps to cores ([Weinberg & Katz 2002](#)). This induces profound changes in the orbits of the dark matter particles in the halo ([Athanasoula 2002](#); [Collier et al. 2019](#)).

Recent data from the third data release (DR3) of *Gaia* ([Gaia Collaboration et al. 2016, 2023a](#)) has revealed previously undetected substructure in the stellar halo of the Milky Way. By plotting Galactocentric radial velocity v_r against Galactocentric radius r , [Belokurov et al. \(2023\)](#) showed that there are multiple ‘chevron’-shaped overdensities in this radial phase space. These bear a close resemblance to structures which result from the phase mixing of debris from a merging satellite on an eccentric or radial orbit ([Fillmore & Goldreich 1984](#); [Dong-Páez et al. 2022](#); [Davies et al. 2023a](#)). [Belokurov et al. \(2023\)](#) showed that they are present at both low and high metallicity, and are still visible when only stars with $[\text{Fe}/\text{H}] > -0.7$ are included. However, stars originating from the Milky Way’s accreted satellites have lower metallicity than this. The *Gaia* Sausage-Enceladus ([Belokurov et al. 2018](#); [Helmi et al. 2018](#)) was one of the most massive mergers in the Milky Way’s history, and its comparatively high metallicity debris dominates the stellar halo in the solar neighbourhood ([Naidu et al. 2020](#)). However, only a very small proportion of its stars have $[\text{Fe}/\text{H}] > -0.7$ ([Naidu et al. 2020](#); [Feuillet et al. 2021](#)). This challenges the assumption that the radial phase space structures are due to accreted material.

There are already indications that bar-driven features in the stellar halo are possible. For example, motivated by the shortness of the Ophiuchus Stream, [Hattori et al. \(2016\)](#) used numerical simulations to show that its properties may have been influenced by its interaction with the bar, despite the Stream stars lying at heights of ≈ 5 kpc above the Galactic plane. [Schuster et al. \(2019\)](#) examined the halo moving groups G18-39 and G21-22 as possible resonant structures generated by the bar – albeit with a pattern speed $45\text{--}55 \text{ km s}^{-1} \text{ kpc}^{-1}$ which is rather high nowadays. These mildly retrograde moving groups were discovered in [Silva et al. \(2012\)](#), who suggested that they may be debris from the unusual and retrograde globular cluster ω Centauri. [Myeong et al. \(2018\)](#) identified the resonance generating the Hercules Stream in the solar neighbourhood as present even in stars with metallicities as low as $[\text{Fe}/\text{H}] \approx -2.9$ and so normally associated with thick disc and halo. Very recently, the interaction of a rotating bar with radial phase space chevrons has been studied by [Davies et al. \(2023b\)](#). They showed that with realistic values of the pattern speed, the bar is capable of blurring and destroying much of the phase space structure resulting from a satellite merger. If a bar can destroy, then it is natural to ask whether it can also create substructure.

In this work, we examine the creation of substructure from a smooth stellar halo via resonances. We identify a prominent ridge in energy and angular momentum space (a proxy for action space)

and show that such a feature is a natural outcome of bar-driven resonances in the stellar halo. The prominence and narrowness of this ridge provides a novel method of measuring the pattern speed of the bar.

The paper is arranged as follows. In Section 2, we summarize the dynamics of orbits in rotating potentials and introduce the principal bar resonances. We use data from *Gaia* DR3 in Section 3 to reveal structures in energy-angular momentum and radial phase space. In Section 4, we describe our simulations of the stellar halo and bar, and compare them to the data. Finally we present our conclusions in Section 5.

2 DYNAMICS IN A ROTATING POTENTIAL

Consider a steady non-axisymmetric potential rotating with pattern speed (angular frequency) Ω_b about the z -axis. Although the energy E and z component of angular momentum L_z of a particle can vary, a linear combination of the two known as the Jacobi integral is conserved ([Binney & Tremaine 2008](#)). This is defined as

$$H_J = E - \Omega_b L_z. \quad (1)$$

The Jacobi integral is the energy in the rotating frame. As the potential is steady in this frame, it follows from time-invariance that the Jacobi integral is conserved. Hence in the E versus L_z plane, stars are constrained to move along straight lines of gradient Ω_b , provided the pattern speed remains steady.

Action-angle coordinates are a set of canonical coordinates useful in nearly integrable systems where most orbits are regular and not chaotic (e.g. [Arnold 1978](#)). Each star is described by three actions J_i which are constant and three angles θ_i which increase linearly with frequencies Ω_i . As an example, a slightly eccentric and inclined orbit in a weakly non-axisymmetric potential can be approximated as motion on an epicycle around a guiding centre. This centre follows a circular orbit in the $z = 0$ plane with azimuthal frequency Ω_ϕ , set by the rotation curve of the potential. The particle oscillates in the (cylindrical polar) R -direction with the epicyclic frequency Ω_R and in the z -direction with the vertical frequency Ω_z . Action-angle coordinates can be computed for general orbits in axisymmetric galactic potentials using modern stellar dynamical packages like AGAMA ([Vasiliev 2019](#)).

The locations of the principal resonances in space is in general hard to establish. Only for orbits confined to the disc plane are matters reasonably straightforward. In the frame corotating with the bar at frequency equal to the pattern speed Ω_b , the mean azimuthal frequency of a star is $\Omega_\phi - \Omega_b$. We define the ratio of frequencies in this frame $r_\Omega \equiv (\Omega_\phi - \Omega_b)/\Omega_R$. An orbit is resonant with the bar if $r_\Omega = \pm n/m$, where n and m are integers. The most important of these are the corotation resonance ($\Omega_\phi = \Omega_b$, $r_\Omega = 0$) and the Lindblad resonances ($r_\Omega = \pm 1/m$) ([Binney & Tremaine 2008](#)). For orbits that explore the stellar halo, the location of the resonances can change with height above or below the Galactic plane ([Moreno et al. 2015a](#); [Trick et al. 2021](#)).

Why are the resonant orbits so important? Suppose a bar-like disturbance rotating at angular frequency Ω_b is applied to the disc. On each traverse, the resonant stars meet the crests and troughs of the perturbation potential at the same spots in their orbits and this causes secular changes in the orbital elements (e.g. [Lynden-Bell 1973](#); [Lynden-Bell & Kalnajs 1972](#); [Collett et al. 1997](#); [Molloy et al. 2015](#)). The non-resonant stars feel only periodic fluctuations that average to zero in the long term. As the strength of the bar’s perturbation increases, stars near the locus of exact resonance are

captured into libration around the parent closed periodic orbit. So, the neighbourhoods of the resonances are the regions of a galaxy where a bar can produce long-lived changes in the stellar populations.

3 DATA

3.1 *Gaia* DR3 RVS sample

We use the sample of stars from *Gaia* DR3 (Gaia Collaboration et al. 2016, 2023a) described by Belokurov et al. (2023) which includes line-of-sight velocity measurements from the Radial Velocity Spectrometer (RVS, Katz et al. 2023). We use distances calculated by Bailer-Jones et al. (2021). This sample has selection cuts on parallax error ($\varpi/\sigma_\varpi > 10$) and heliocentric distance ($D < 15$ kpc). All sources within 1.5° of known globular clusters closer than 5 kpc have been removed (Belokurov et al. 2023). This leaves ~ 25 million sources out of the ~ 34 million with line-of-sight velocity measurements. For Section 3.4 we further limit our sample to stars with metallicity ([Fe/H]) values calculated by Belokurov et al. (2023). These were derived from BP/RP spectra calibrated with data from APOGEE DR17 (Abdurro'uf et al. 2022). See Belokurov et al. (2023) for a detailed description. This provides us with a final sample of 22.5 million sources, all with 6D phase space and [Fe/H] measurements.

We transform the positions and velocities into a Galactocentric left-handed coordinate system in which the Sun's position and velocity are $(x_\odot, y_\odot, z_\odot) = (8, 0, 0)$ kpc and $(v_{\odot x}, v_{\odot y}, v_{\odot z}) = (-9.3, 251.5, 8.59)$ km s $^{-1}$ (as reported by Gaia Collaboration et al. 2023b). The x - y and R - z distributions of this sample are shown in Fig. 1.

3.2 RVS sample weighting

To correct for selection effects arising from the RVS and parallax error cuts, we apply a weighting to the data points. This is based on the ratio of our sample size to the total sample size of stars with photo-geometric distance measurements, as a function of r . This procedure is described in detail below.

We find the distributions in r of sources in DR3 with non-zero photo-geometric distance (Sample A), and also those with $\varpi/\sigma_\varpi > 10$ and non-zero RVS error (Sample B; similar to the final sample we use without more specific cuts). To undo this effect we calculate the ratio of the two distributions as a function of r . This ratio (Sample B/Sample A) can be seen in the top panel Fig. 2. Due to the RVS and parallax error cuts, this ratio has a strong peak around the Sun ($r \approx 7 - 9$ kpc), which will likely cause spurious peaks in the energy distribution. We therefore weight our data points by the ratio Sample A/Sample B to undo the RVS and parallax error selection effects. The bottom panel of Fig. 2 shows that this weighting largely removes the strong peak in the distribution of r in our sample around the Sun, leaving a much flatter distribution.

The results can be seen in the lower two panels of Fig. 3 and in the left-hand column of Fig. 4. In the latter case the overdensity at $r = 8$ kpc (see Belokurov et al. 2023) is almost completely removed, resulting in a much more informative distribution. For the energy-angular momentum distributions (Figs. 3 and 15) we set the weighting to zero wherever it exceeds 200 (i.e. where the function in Figs. 2 is less than 0.005). This removes stars whose weighting is extremely large due to low sample density, and is equivalent to removing stars at $r \lesssim 5$ kpc and $r \gtrsim 11$ kpc.

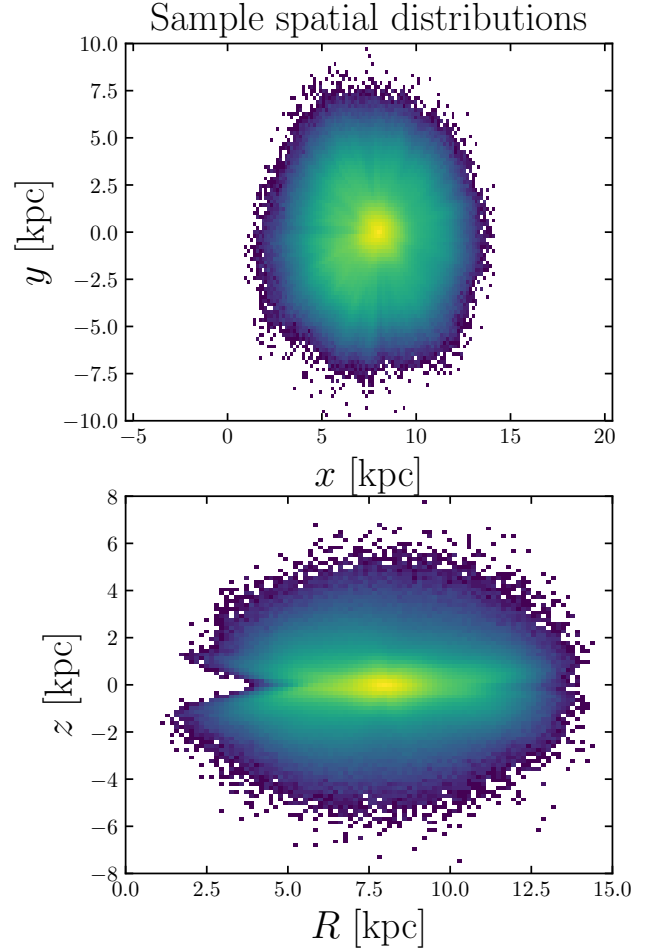


Figure 1. Distributions of our *Gaia* DR3 sample in Galactocentric Cartesian coordinates (top panel) and cylindrical coordinates (bottom panel). The Sun is located at $x = R = 8$ kpc, $y = z = 0$ kpc.

3.3 Energy-angular momentum space

The plot of energy E versus z -component of the angular momentum L_z is a good approximation to action space (J_r, J_ϕ). This is because energy is a proxy for radial action J_r , whilst L_z is the azimuthal action J_ϕ in nearly axisymmetric potentials.

To calculate estimates of the energies E of the stars in our sample, we use a modified version of the potential `MWPotential2014` described in Bovy (2015). Similarly to Belokurov et al. (2023), we set the virial mass of the Navarro-Frenk-White dark matter halo to $1 \times 10^{12} M_\odot$, the virial radius to 260 kpc and the concentration to 18.8, which gives a circular velocity at the Sun's radius of about 235 km s $^{-1}$ (c.f. Bland-Hawthorn & Gerhard 2016).

The distribution of E versus L_z is plotted in the top panel of Fig. 3. The left-handed coordinate system means that stars in the disc have $L_z > 0$. The second panel shows the same distribution after unsharp masking has been applied in E to reveal details of the distribution more clearly. Alternating overdensities (black) and underdensities (white) are seen most prominently at $L_z > 0$ with roughly constant energy.

The weighted distributions are shown in the third and fourth panels of Fig. 3. The weighting has mostly removed the energy ridge at $E \approx -1.5 \times 10^5$ km 2 s $^{-2}$, indicating that this resulted from selection

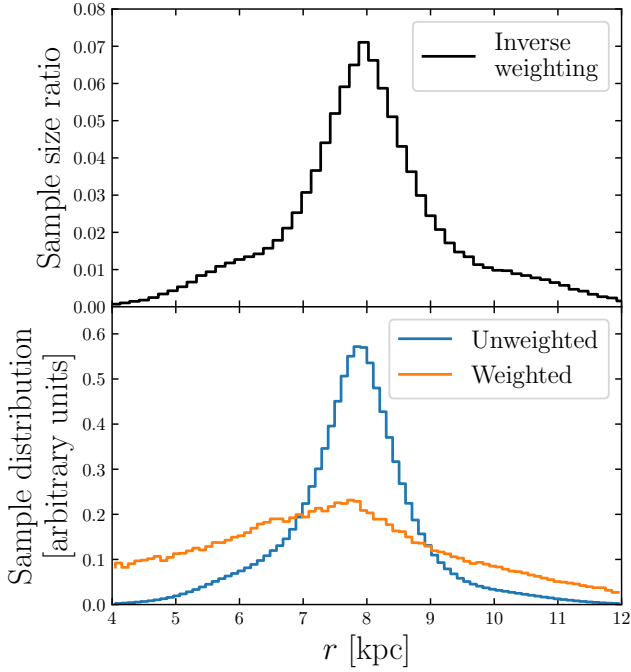


Figure 2. Top panel: The inverse of the weighting function against Galactocentric radius r . This is the ratio of the size of the RVS sample with a parallax error cut applied ($\varpi/\sigma_\varpi > 10$) to the size of the DR3 sample with photo-geometric distance measurements. There is a strong peak between 7 and 9 kpc due to the high concentration of the former sample around the Sun. **Bottom panel:** histograms of the unweighted (blue) and weighted (orange) r distributions of our sample. This demonstrates that the weighting largely removes the strong peak around the Sun at $r = 8$ kpc.

effects. However, the highest energy ridge at $E \approx -1.4 \times 10^5 \text{ km}^2 \text{ s}^{-2}$ remains, suggesting that this is a genuine feature of the distribution. It can also be seen in the dissection of the stellar halo in action space by Myeong et al. (2018), albeit with a much smaller dataset.

3.4 Radial phase space

To isolate the region of E - L_z space where the ridge is most prominent, we apply an angular momentum cut to include only stars with $0.25 \times 10^3 < L_z [\text{kpc km s}^{-1}] < 1.0 \times 10^3$. We have checked that the results are not sensitive to the exact choice of L_z cut.

We calculate the Galactocentric spherical radii and radial velocities (r, v_r) for each particle. The (r, v_r) distributions are shown in Fig. 4 for stars with $[\text{Fe}/\text{H}] < -0.7$ (top row) and $[\text{Fe}/\text{H}] > -0.7$ (bottom row). While the low metallicity sample contains a mix of accreted and *in situ* stars (Belokurov & Kravtsov 2022; Conroy et al. 2022; Myeong et al. 2022), $[\text{Fe}/\text{H}] > -0.7$ is dominated by *in situ* stars (Belokurov et al. 2023). We use the weighting described above in the left-hand column, and in the right-hand column we normalise the histograms so that each column of pixels has the same total count.

The chevron-shaped ridges reported by Belokurov et al. (2023) are visible, particularly for $[\text{Fe}/\text{H}] < -0.7$. For both metallicity cuts the most prominent feature is a roughly triangular overdensity reaching a maximum radius of ~ 7 kpc. We find that its position and size is highly dependent on the choice of L_z cut used, and it coincides with the sloping low energy overdensity at the edge of the E - L_z distribution in Fig. 3. This therefore consists mostly of stars on close

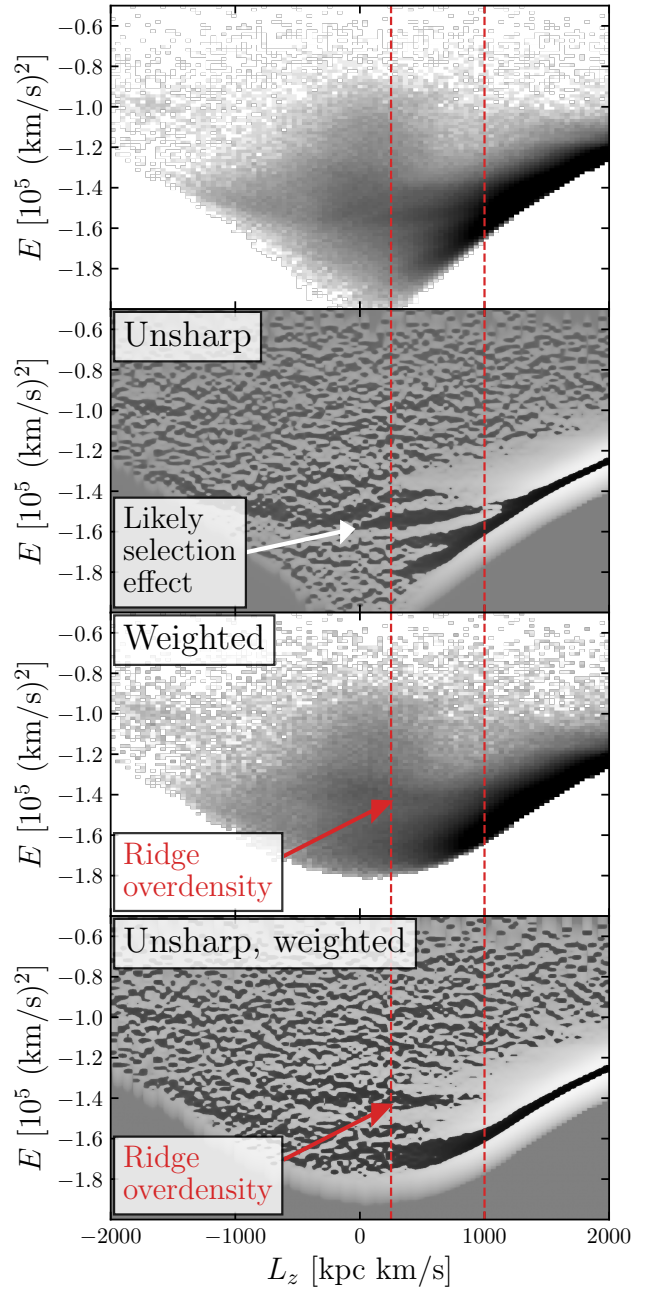


Figure 3. Top panel: distribution of energy E vs angular momentum L_z , where prograde orbits have $L_z > 0$. The red dashed lines mark the angular momentum cut used in Fig. 4. The highly populated disc can be seen on the right-hand side of the distribution. **2nd panel:** as above, but with unsharp filtering applied; a background smoothed with a Gaussian kernel in E has been subtracted off. We use 100 pixels along the E -axis, and the Gaussian kernel has a standard deviation of 2 pixels. Black (white) pixels denote overdensities (underdensities). This reveals several ridges at roughly constant energy with mostly $L_z > 0$. **Bottom two panels:** As above, but all data points are weighted based on the number of stars in the RVS sample as a function of radius. This largely removes the ridge at $E \approx -1.5 \times 10^5 \text{ km}^2 \text{ s}^{-2}$, which was likely due to a selection effect. The highest energy ridge (at $E \approx -1.4 \times 10^5 \text{ km}^2 \text{ s}^{-2}$) remains.

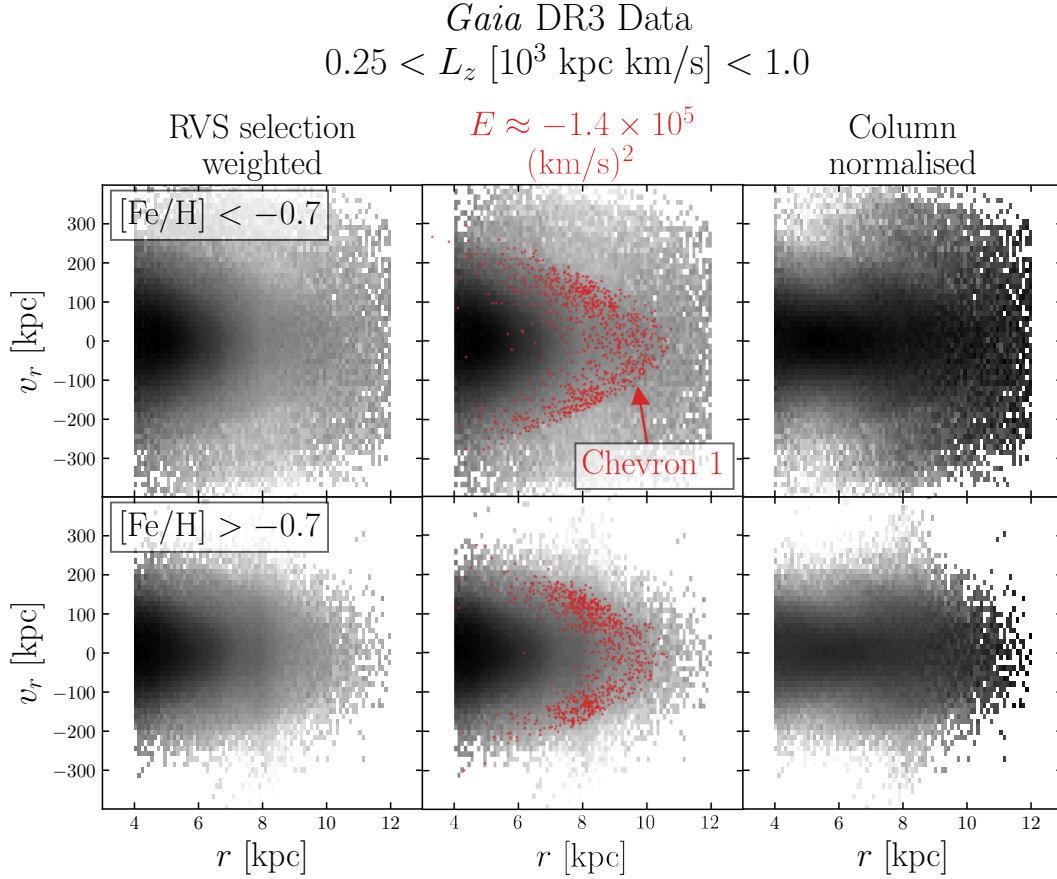


Figure 4. Radial phase space of the DR3 RVS sample, with an L_z cut applied. The top (bottom) row shows low (high) metallicity stars, with the threshold set at $[\text{Fe}/\text{H}] = -0.7$. The high metallicity sample is dominated by *in situ* stars. In the middle column, we plot the positions of particles with energy $E \approx -1.4 \times 10^5 \text{ km}^2 \text{ s}^{-2}$, which corresponds to the horizontal ridge in E - L_z space (Fig. 3). In the right-hand column, we column-normalise the histograms (i.e. each column of pixels has the same total count). In the top row, several chevron-shaped overdensities are visible, the most prominent of which (peaking at $r \approx 10.5 \text{ kpc}$) is also visible at high metallicity. As shown by the middle column, this corresponds to the energy of the horizontal overdensity in Fig. 3. Following Belokurov et al. (2023), we denote this feature ‘Chevron 1’. The dark region (at $r \lesssim 7 \text{ kpc}$) is due to the disc, and moves depending on the L_z cut.

to circular orbits in the disc. Its shape depends on the L_z cut because the energy of disc orbits is L_z -dependent.

More interestingly, there is a second fainter chevron that reaches $\approx 10.5 \text{ kpc}$, corresponding to ‘Chevron 1’ described by Belokurov et al. (2023). This is a sharp edge in the distribution, outside of which the density of stars is lower. This is visible for both metallicity cuts, albeit more faintly at $[\text{Fe}/\text{H}] > -0.7$ (also see the bottom-left panel of Fig. 8 in Belokurov et al. 2023). We have found that the position of this chevron is independent of the exact L_z cut used. This suggests that the orbital energies of its stars have little L_z dependence (by contrast to the disc). We therefore postulate that it is a manifestation of the horizontal overdensity in Fig. 3 at $E \approx -1.4 \times 10^5 \text{ km}^2 \text{ s}^{-2}$. To test this we plot the phase space positions of particles with energies very close to this in the middle column of Fig. 4. These particles form a chevron with its outer edge closely lining up with the edge of Chevron 1. This strongly suggests that the energy ridge and chevron are indeed different representations of the same entity. The fact that these stars span a wide range of radii indicates that this overdensity is not merely due to a radial selection effect around the Sun.

In summary, this is a feature at fixed energy, comprised of particles on mostly prograde orbits with a range of L_z . The radial phase space shows that they have apocentres of up to $\approx 10 \text{ kpc}$. Belokurov et al. (2023) suggested that this and other chevrons arose from the phase-

mixing of the debris from a massive satellite which merged with the Milky Way, possibly the GSE. However, the presence of Chevron 1 at high $[\text{Fe}/\text{H}]$ challenges this hypothesis, since very few GSE stars have such high metallicities (Belokurov et al. 2023).

3.5 Configuration and frequency space

We examine the distribution of stars in the E - L_z overdensity as follows. We select stars in the angular momentum range $0.25 < L_z [10^3 \text{ kpc km s}^{-1}] < 1.0$ (between the red dashed lines in Fig. 3), and with energies between $E = (-1.4 \pm 0.02) \times 10^5 \text{ km}^2 \text{ s}^{-2}$. This isolates the clear ridge in the bottom panel of Fig. 3. We plot the cylindrical coordinates (R, z) of this sample in Fig. 5. This demonstrates the large vertical extent of the distribution of stars in this overdensity. While our sample as a whole has a large contribution from the disc at $|z| \lesssim 1$ (see Fig. 1), no such excess is apparent in Fig. 5. This suggests that this part of the overdensity is comprised largely of stars on halo orbits. We note that more disc stars would be present if we increased the upper bound of our L_z cut to include orbits with low eccentricity and inclination. However, in this study we focus on the halo-like orbits at lower L_z .

We wish to consider whether the overdensity could be associated with a resonance with the bar. We therefore calculate the orbital fre-

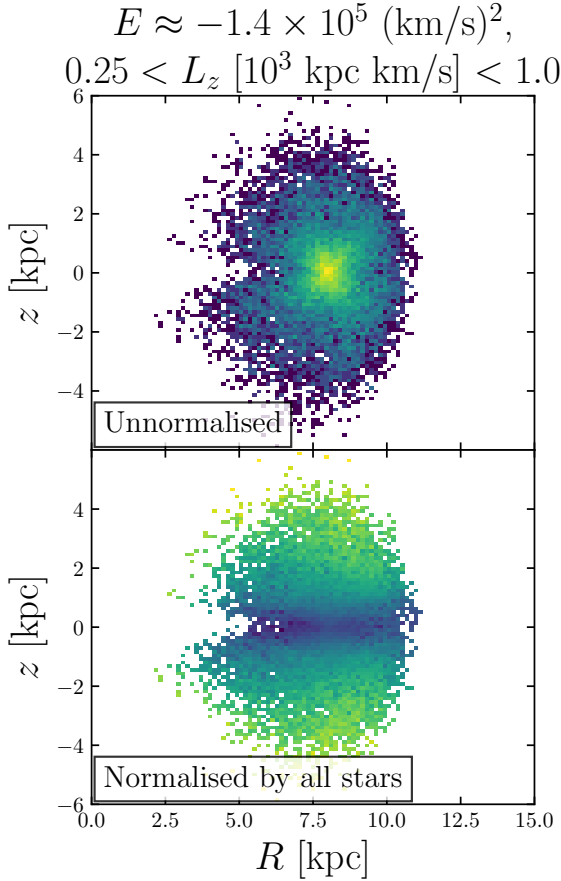


Figure 5. Radial and vertical distribution of stars close to the ridge at $E = -1.4 \times 10^5 \text{ km}^2 \text{ s}^{-2}$, within the angular momentum cut $0.25 < L_z [10^3 \text{ km s}^{-1}] < 1.0$. In the bottom panel the distribution is normalised by the R - z distribution of all stars in the sample. The selected stars are spread over a wide range of z , with no large excess close to $z = 0$ (other than near the Sun). This is emphasised by the lower panel, which shows the depletion of stars near the disc compared to the sample as a whole. The overdensity therefore has a large contribution from the stellar halo.

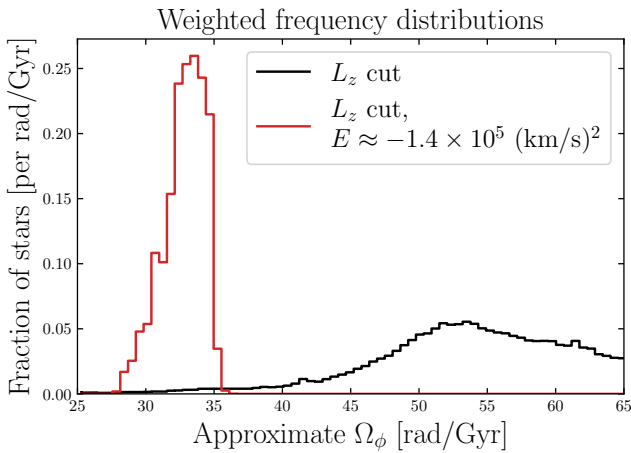


Figure 6. Distributions of the azimuthal frequency Ω_ϕ within the angular momentum cut $0.25 < L_z [10^3 \text{ km s}^{-1}] < 1.0$. The black histogram shows all stars, and the red shows those with energies close to $E = -1.4 \times 10^5 \text{ km}^2 \text{ s}^{-2}$. We have applied the weighting discussed in Section 3.2. Stars close to the energy overdensity have frequencies strongly peaked around 34 rad Gyr^{-1} , similar to some estimates of the bar's pattern speed.

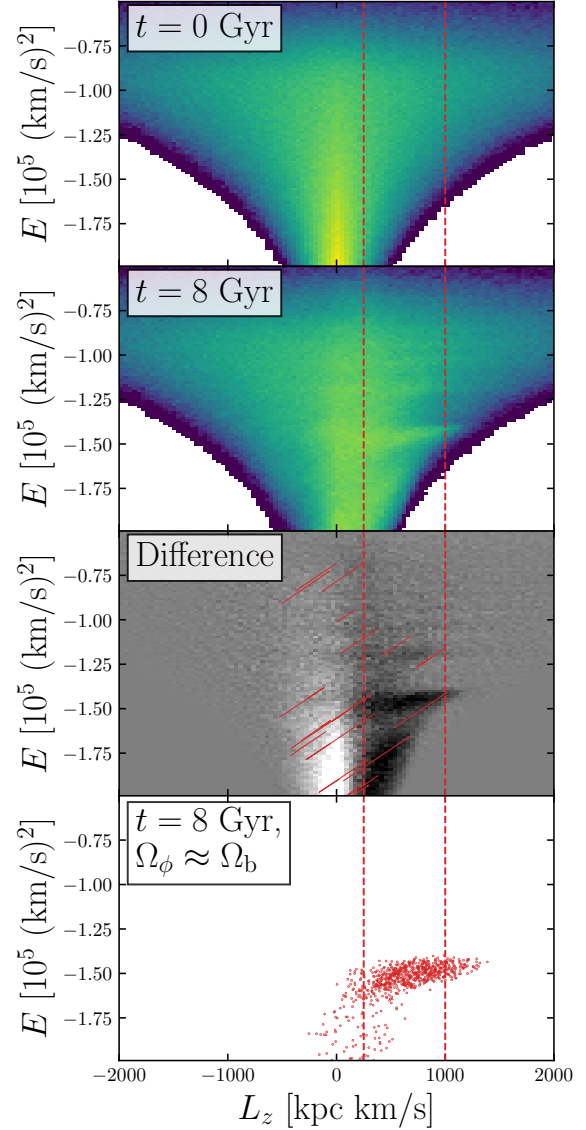


Figure 7. Top two panels: Distributions of E and L_z of the star particles at the beginning and end of the simulation. The colour map uses the same logarithmic normalisation for each panel, and as in Fig. 3 the red dashed lines mark the L_z cut. After the growth of the bar, ridge-like overdensities at certain energies emerge from the initially smooth distribution. These are at $L_z > 0$ (i.e. orbiting in the same direction as the bar's rotation). **3rd panel:** Difference between the $t = 0$ and later distributions. Black (white) pixels mark where the density has increased (decreased). This emphasises that particles have moved away from $L_z \approx 0$ and $L_z < 0$ into the ridges at $L_z > 0$. The red diagonal streaks mark the paths taken by a selection of particles, and have gradients close to the pattern speed. **Bottom panel:** stars close to the corotation resonance ($\Omega_\phi = \Omega_b$) at the end of the simulation. These are almost all located within the lowest energy overdensity at $E \approx -1.5 \times 10^5 \text{ km}^2 \text{ s}^{-2}$, strongly implying that this overdensity is a manifestation of this resonance.

quencies $\Omega_i \equiv \partial H / \partial J_i$ of the stars in the axisymmetric potential. Here H is the Hamiltonian and J_i are the actions, calculated using the Stäckel approximation (see e.g. de Zeeuw 1985; Sanders & Binney 2016). We show the distributions of the azimuthal frequency Ω_ϕ in Fig. 6 for stars within the L_z cut described above, weighted as outlined in Section 3.2. All stars within the cut are included in the

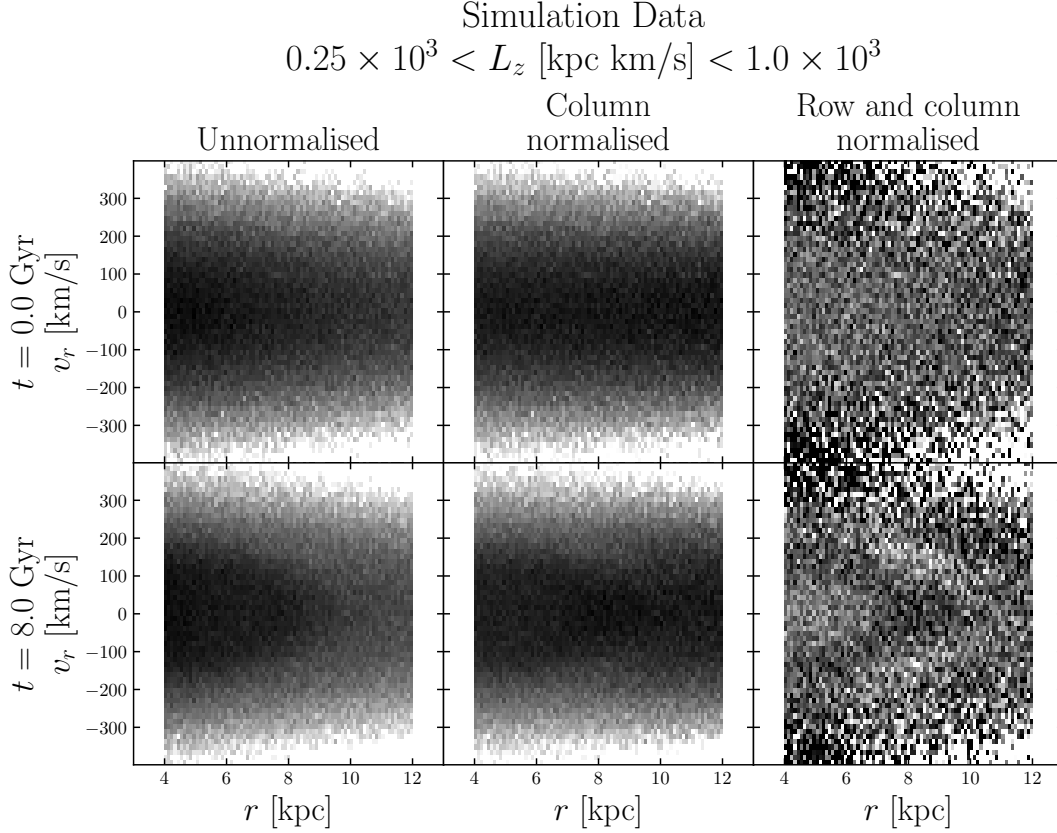


Figure 8. Radial phase space of the simulated stars, with the same L_z cut as used on the data in Fig. 4. The top and bottom rows show the start and end of the simulation respectively. From left to right, the columns are unnormalised, normalised by column, and normalised by both row and column. The distribution is initially smooth, with no structure visible. However, at the end of the simulation after the growth of the bar, a wedge-shaped overdensity with its tip at ~ 10 kpc is visible. This is revealed more clearly in the right-hand column, and bears a close resemblance to Chevron 1 seen in the data in Fig. 4.

black histogram, while the stars close to $E = -1.4 \times 10^5 \text{ km}^2 \text{ s}^{-2}$ are shown in red. The stars in this overdensity have frequencies strongly peaked around 34 rad Gyr^{-1} , similar to some recent estimates of the pattern speed of the bar (e.g. Binney 2020). This suggests that this overdensity may be associated with the bar’s corotation resonance. We note however that the true frequencies in a rotating barred potential may differ somewhat to these estimates, so simulations with a bar are necessary for a more accurate comparison. This is what we proceed to carry out in Section 4.

4 SIMULATIONS

We now investigate whether such a feature with the above properties can instead be produced by a rotating bar via resonant trapping. We run test particle simulations of a stellar halo-like population of particles using the galactic dynamics package AGAMA (Vasiliev 2019). We initialise this population from a steady-state distribution function in the axisymmetric Milky Way potential described in Section 3.3, before introducing a rotating bar-like perturbation which smoothly increases in strength.

4.1 Barred potential

To represent a bar, we use the Dehnen (2000) model generalised to 3 dimensions by Monari et al. (2016). This consists of a quadrupole per-

turbation to the potential, written in cylindrical coordinates (R, ϕ, z) in the form

$$\Phi_b = A_b(t) \cos(2[\phi - \phi_b(t)]) \left(\frac{R}{r}\right)^2 \times \begin{cases} (r/R_b)^3 - 2 & r < R_b \\ -(R_b/r)^3 & r \geq R_b, \end{cases} \quad (2)$$

where $r^2 = R^2 + z^2$. We increase the amplitude of the perturbation $A_b(t)$ smoothly between times t_0 and t_1 according to

$$A_b(t) = A_f \left(\frac{3}{16} \xi^5 - \frac{5}{8} \xi^3 + \frac{15}{16} \xi + \frac{1}{2} \right), \quad (3)$$

$$\xi \equiv 2 \frac{t - t_0}{t_1 - t_0} - 1. \quad (4)$$

For $t < t_0$ and $t > t_1$, A_b equals 0 and A_f respectively. Following Dehnen (2000), we parameterise the bar perturbation amplitude with the bar strength

$$\alpha \equiv 3 \frac{A_f}{v_0^2} \left(\frac{R_b}{R_0} \right)^3, \quad (5)$$

where v_0 is the circular velocity at $R_0 \equiv 8 \text{ kpc}$. We rotate this potential at constant pattern speed Ω_b . We compare simulations with pattern speeds of $\Omega_b = \{35, 40, 45\} \text{ km s}^{-1} \text{ kpc}^{-1}$, but focus on the $\Omega_b = 40 \text{ km s}^{-1} \text{ kpc}^{-1}$ model for most of this section. This is close to many recent estimates of the bar’s pattern speed (e.g. Wang et al. 2013; Portail et al. 2017; Sanders et al. 2019; Binney 2020).

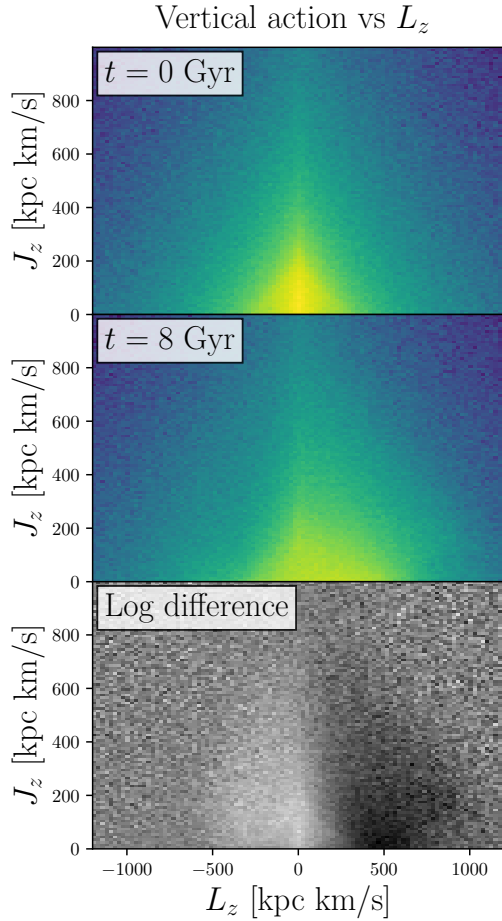


Figure 9. Vertical action J_z vs angular momentum L_z at the beginning and end of the simulation. The bottom panel shows the ratio of the two histograms, where black (white) pixels show where the density has increased (decreased). This indicates that stars at low J_z are more likely to be pushed to high L_z by the bar.

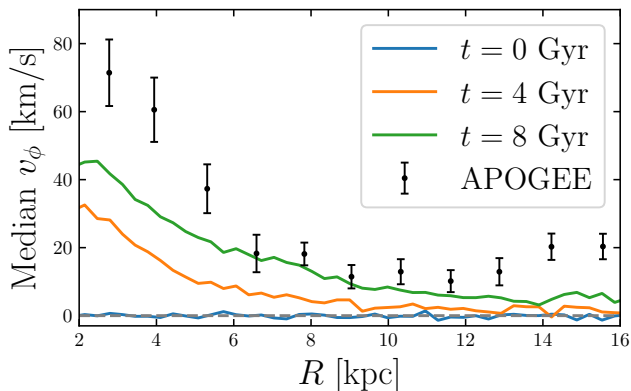


Figure 10. Median azimuthal velocity $\langle v_\phi \rangle$ as a function of cylindrical radius R in each snapshot of the simulations (coloured lines) compared to observed values for low $[\text{Fe}/\text{H}]$ stars from APOGEE DR17 (black points). While initially the halo has no net spin, after the bar grows the mean azimuthal velocity is positive, particularly inside 8 kpc. The observed values show a similar trend, albeit with a higher median v_ϕ .

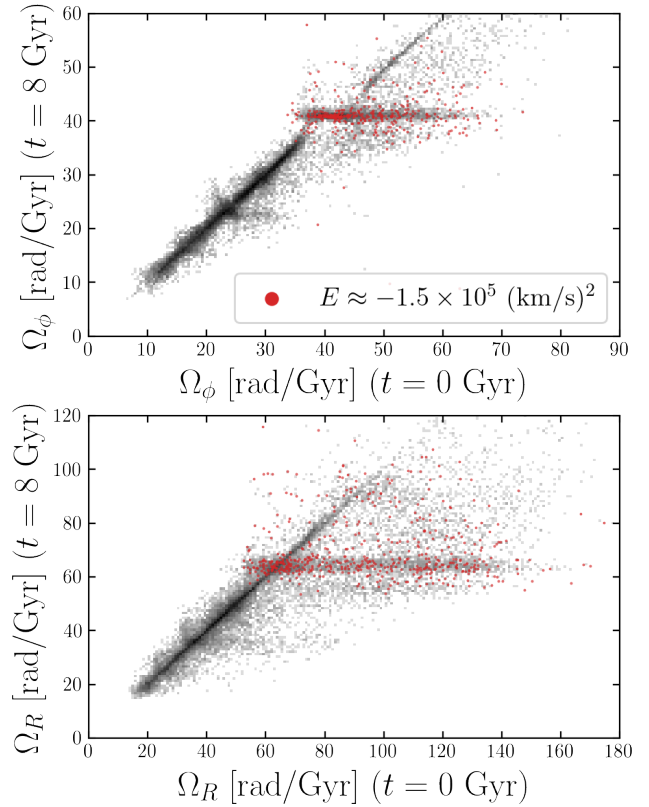


Figure 11. Top panel: initial (x-axis) and final (y-axis) azimuthal frequencies Ω_ϕ of simulated stars. These are calculated by integrating orbits from the initial and final phase space positions in a potential of constant pattern speed. The red points show stars with final energy close to $E = -1.5 \times 10^5 \text{ km}^2 \text{ s}^{-2}$, the approximate energy of the most prominent overdensity in Fig. 7. **Bottom panel:** as above, but instead showing radial frequencies Ω_R . In both cases horizontal stripes indicate that the final frequencies are highly clustered about certain values. These include $\Omega_\phi = 40 \text{ km s}^{-1} \text{ kpc}^{-1}$, the bar pattern speed. Most of the red points lie close to this frequency, showing that this corresponds to the prominent energy overdensity in Fig. 7.

We set $\alpha = 0.01$ following [Dehnen \(2000\)](#), $t_0 = 2$ Gyr and $t_1 = 4$ Gyr, so the bar grows over a period of 2 Gyr. We run the simulation between $t = 0$ and $t_f = 8$ Gyr. This is roughly the duration of the period of the Milky Way’s history since the GSE merger, over which no major satellite has been accreted (e.g. [Belokurov et al. 2018](#); [Kruijssen et al. 2020](#)). We set the bar radius to $R_b = 2$ kpc. While this is likely smaller than the Milky Way’s bar at present (e.g. [Hammersley et al. 1994](#); [Wegg et al. 2015](#); [Lucey et al. 2023](#)), it may be more realistic for the period over which it was formed ([Rosas-Guevara et al. 2022](#)).

4.2 Distribution function

We generate a halo-like population of stars using the double power law distribution function implemented in AGAMA by [Vasiliev \(2019\)](#), which is a generalisation of ones introduced by [Posti et al. \(2015\)](#) and [Williams & Evans \(2015\)](#):

$$f(\mathbf{J}) = \frac{M}{(2\pi J_0)^3} \left[1 + \left(\frac{J_0}{h(\mathbf{J})} \right)^\eta \right]^{\Gamma/\eta} \left[1 + \left(\frac{h(\mathbf{J})}{J_0} \right)^\eta \right]^{-B/\eta}, \quad (6)$$

$$h(\mathbf{J}) \equiv J_r + |J_\phi| + J_z. \quad (7)$$

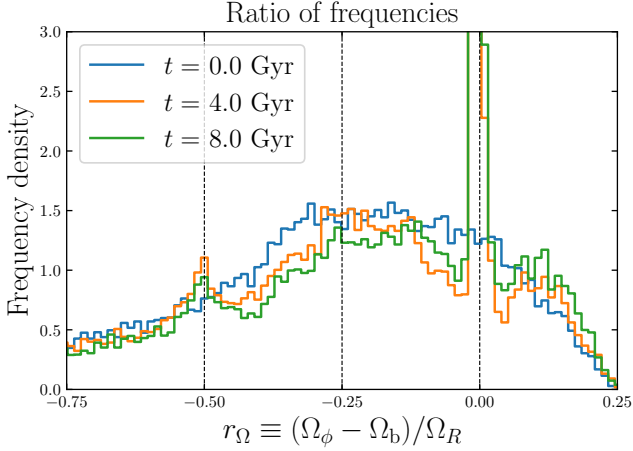


Figure 12. Distributions of r_Ω , the ratio of azimuthal to radial frequencies in the frame rotating at the pattern speed Ω_b , at three snapshots. The distributions at $t = 4$ and 8 Gyr have clear resonant peaks at $r_\Omega = 0$ (corresponding to corotation) and $r_\Omega = -0.5$ (the outer Lindblad resonance). The $r_\Omega = -0.25$ or ultraharmonic resonance is also marked, although the peak is weaker here.

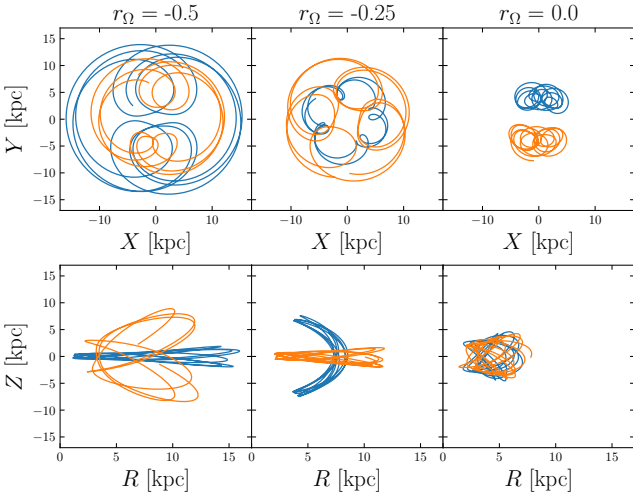


Figure 13. Orbits close to each of the three resonances marked above, plotted in the frame corotating with the bar. The Galactic disc lies in the $X - Y$ plane, with the bar’s major axis along the X -axis. The bottom row shows the height above the disc Z vs cylindrical radius R . The two colours show two separate orbits at each resonance. These demonstrate that trapped orbits can be both disc-like (e.g. orange, middle column) or halo-like, with large vertical excursions (e.g. orange, left-hand column).

Here, J_0 is the characteristic total action $|J|$ of orbits near the break radius of the double-power law profile (Posti et al. 2015).

We wish to choose values of J_0 and the power law indices Γ and B to roughly reproduce the density profile of the Milky Way’s stellar halo. Multiple studies have found that the density profile can be fitted by a double power law with inner slope $\gamma \sim 2.5$ and outer slope $\beta \sim 4.5$, with a break radius at $r \approx 25$ kpc (e.g. Watkins et al. 2009; Deason et al. 2011; Faccioli et al. 2014; Pila-Díez et al. 2015). We find that choosing $J_0 = 3500$ kpc km s $^{-1}$ and $(\Gamma, B) = (2.4, 4.6)$ roughly recovers the values for the Milky Way. We set the steepness

of the break to $\eta = 10$, which results in the density power law slope changing between radii of $\sim 10 - 40$ kpc.

4.3 Results

We integrate the orbits of these stars in the combined potential of the Milky Way and the growing rotating bar for time t_f . We calculate the energy E and angular momentum L_z of the star particles in each snapshot, and show these distributions in Fig. 7. At the beginning of the simulation, there is a large concentration of stars at small L_z but otherwise no structure. However, at $t = 4$ and 8 Gyr horizontal striations are visible at $L_z > 0$, corresponding to specific energies where there are overdensities and underdensities of stars. These stripes resemble those seen in the data in Fig. 3, as they occupy a similar region of E - L_z space. Since the initial distribution function is symmetric in L_z , the fact that these simulated ridges occur only at $L_z > 0$ implies that they must be related to the rotation of the bar.

The third panel of Fig. 7 shows how the star particles move through E - L_z space. The red streaks mark the paths taken by a selection of stars, where the motion is towards the top-right. This results in a depletion of stars at $L_z \leq 0$ (white pixels) and an enhancement in their density in the ridges at $L_z > 0$. This behaviour strongly resembles that expected for a steady but rotating non-axisymmetric potential, where stars are constrained to move along lines of gradient Ω_b in the E vs L_z plane due to conservation of the Jacobi integral. We see similar behaviour here, though we note that the bar perturbation grows in magnitude between $t = 2$ and 4 Gyr, so the Jacobi integral is not exactly conserved during this period. We have checked that the gradient of these streaks is indeed approximately Ω_b .

We calculate the instantaneous radial and azimuthal frequencies of the star particles as follows. We integrate their orbits from their phase space positions in each snapshot, using the corresponding potential with constant pattern speed. The frequencies are calculated from the radial and azimuthal motion averaged over several orbital periods. In the bottom panel of Fig. 7 we plot only particles with azimuthal frequencies satisfying $|\Omega_\phi - \Omega_b|/\Omega_b < 0.001$ (i.e. stars very close to the corotation resonance). The distribution of these stars exactly coincides with the lowest energy overdensity seen in the panel above, at $E \approx -1.5 \times 10^5$ km 2 s $^{-2}$. This overdensity can therefore be associated with the corotation resonance.

We show the radial phase space of the simulations in Fig. 8, where we have applied the same radius and angular momentum cuts as in the data in Fig. 4 ($4 < r$ [kpc] < 12 , $0.25 \times 10^3 < L_z$ [kpc km s $^{-1}$] $< 1.0 \times 10^3$). The top and bottom rows show the start and end of the simulation, at $t = 0$ and 8 Gyr respectively. The three columns use different normalisations.

The initial distribution function has a smooth radial phase space, with no substructure visible. However, by the end of the simulation a wedge-shaped overdense region emerges, with its tip at $r \approx 10$ kpc. This bears a strong resemblance to Chevron 1 visible in the data in Fig. 4

To assess how the change in L_z depends on the amplitude of vertical motion of the stars, we calculate the vertical actions J_z using the Stäckel Fudge approximation (Binney 2012) in an axisymmetrised potential (without the bar). The distributions of J_z vs L_z are shown in Fig. 9 at the beginning and end of the simulation. The bottom panel shows the ratio of the two distributions (i.e. the difference in log density). As expected from Fig. 7, at the end of the simulation the average L_z is positive, as stars move away from around $L_z = 0$. Fig. 9 shows that this has J_z dependence, with particles at low J_z experiencing greater increases in L_z on average. This is likely to be

in part due to the fact that stars at low J_z tend to have lower energy and hence interact more strongly with the bar.

Fig. 9 demonstrates that the bar is capable of creating a population of stars with low J_z and positive mean L_z from an initially non-rotating distribution. We note that this bears some similarity to the population ultra metal-poor stars discussed by Sestito et al. (2019). A significant fraction of these stars are on prograde orbits with $J_z \lesssim 100 \text{ kpc km s}^{-1}$, comparable to the distribution in the middle panel of Fig. 9. Our results suggest that the Milky Way’s bar could be responsible for creating the observed distribution of these stars and thus alleviate the need to invoke an early emergence of a prehistoric metal-poor disc (see e.g. Sestito et al. 2019; Di Matteo et al. 2020; Mardini et al. 2022).

We compute the spherically averaged median azimuthal velocity v_ϕ as a function of cylindrical radius R . This is plotted in Fig. 10 at three snapshots. The distribution changes from having no net spin to having a positive median v_ϕ , with larger values at small radii. This is expected from Figs. 7 and 9, which show that by $t = 8 \text{ Gyr}$ there is an excess of star particles at $L_z > 0$, particularly at low energies.

In Fig. 10 we also plot data from data release 17 (DR17) of the APOGEE survey (Majewski et al. 2017; Abdurro’uf et al. 2022) for comparison. We follow closely the steps outlined in Belokurov & Kravtsov (2022) to select unproblematic red giants stars with small chemical and kinematic uncertainties. In addition, we apply $[Al/Fe] < 0.1$ and $[Fe/H] < -1.2$ cuts to limit our sample to predominantly accreted halo stars. These APOGEE low-metallicity data points qualitatively follow a similar trend to the simulation, with a decreasing median v_ϕ with increasing R .

In Fig. 11, we plot the final versus initial values of Ω_ϕ and Ω_R for the simulated star particles with the L_z and r cuts used for Fig. 8. While many particles’ frequencies do not change between the start and end of the simulation, narrow horizontal stripes in the panels of Fig. 11 indicate that the final frequency distributions are tightly clustered around particular values. This includes $\Omega_\phi = 40 \text{ km s}^{-1} \text{ kpc}^{-1}$, which is equal to the pattern speed of the bar. Hence these particles are trapped around the corotation resonance. The red points show particles with energies close to that of the lowest energy overdensity in Fig. 7. Many of these are located at or very close to the corotation resonance, as expected from Fig. 7. To show this and other resonances more clearly we compute the ratio of azimuthal and radial frequencies in the frame corotating with the bar, $r_\Omega \equiv (\Omega_\phi - \Omega_b)/\Omega_R$. The distributions of this quantity are plotted in Fig. 12 at three different times.

This shows that the frequencies are clustered around multiple resonances with the bar. While the initial distribution is relatively smooth, the intermediate and final distributions have multiple sharp peaks located at particular values of r_Ω . This includes the corotation resonance $r_\Omega = 0$ and the outer Lindblad resonance $r_\Omega = -0.5$, with the corotation peak begin particularly strong. The distributions at 4 and 8 Gyr are very similar, showing that the trapping takes place during the growth phase of the bar ($2 < t/\text{Gyr} < 4$) and that the resonant peaks are largely unchanged while the bar is steadily rotating with constant strength.

We show a selection of orbits near three of the resonances in Fig. 13. The top row shows the orbits in the plane of the disc in the frame corotating with the bar (whose major axis lies along the X -axis). Stars near the corotation resonance (right-hand column) do not cross the bar’s major axis, instead orbiting on one side only. The bottom row shows the vertical vs radial behaviour of the orbits. While some resonant orbits remain close to the disc ($Z = 0$ plane), others have large vertical excursions, reaching over 5 kpc above and below the disc. Hence we see that stars on halo-like orbits can contribute

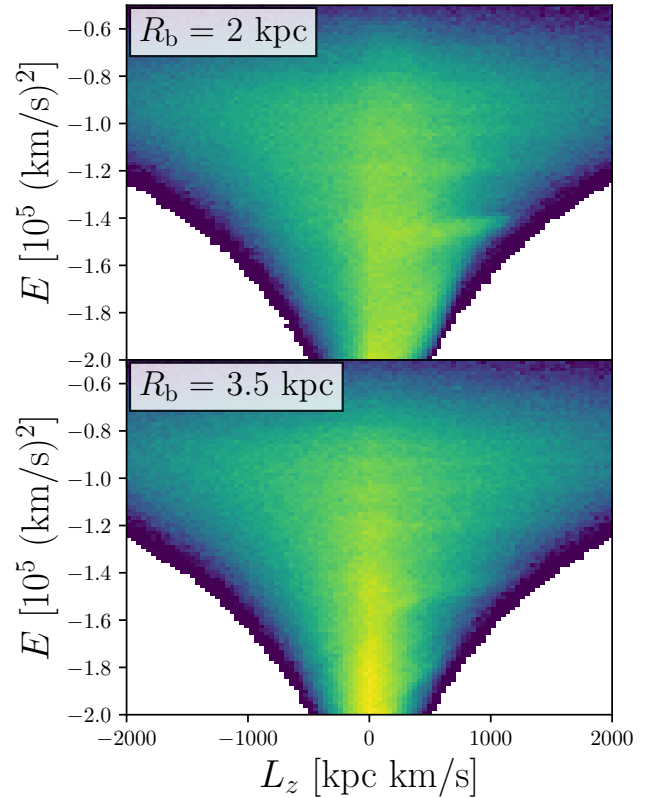


Figure 14. Energy-angular momentum space at the end of the simulation with a bar length of $R_b = 2 \text{ kpc}$ (top panel) and 3 kpc (bottom panel). The overdensities are still clearly visible with the longer bar, albeit with somewhat lower contrast.

to the resonant peaks seen in Fig. 12. Note that the blue orbit in the middle column also has a resonance between its R and Z motion.

4.3.1 Dependence on bar length

To check how our results depend on the bar length R_b , we run another simulation with $R_b = 3.5 \text{ kpc}$. This is the value used by Monari et al. (2016), and is a good fit to the current (rather than initial) size of the Milky Way’s bar. We maintain a bar strength of $\alpha = 0.01$, so the strength of the perturbation near the Sun is unchanged. We show a comparison of the E - L_z space of the two simulations in Fig. 14.

We see that the ridge overdensities with roughly constant energy at $L_z > 0$ remain visible with the longer bar. They are slightly less prominent than with $R_b = 2 \text{ kpc}$, with fewer stars being moved away from $L_z \approx 0$. However, the energies of the overdensities are unaffected by the change in bar size, so our analysis is independent of the exact choice of bar model. We also note that the strength of the overdensities can be changed by a time-dependent pattern speed through the process of resonance sweeping (see e.g. Chiba et al. 2021). We plan to address this in a future work.

4.4 Comparison with data

We wish to estimate the approximate pattern speed of the bar which can best reproduce the observed structures in Fig. 3. For this purpose, we run simulations with constant pattern speeds $\Omega_b = \{35, 40, 45\}$

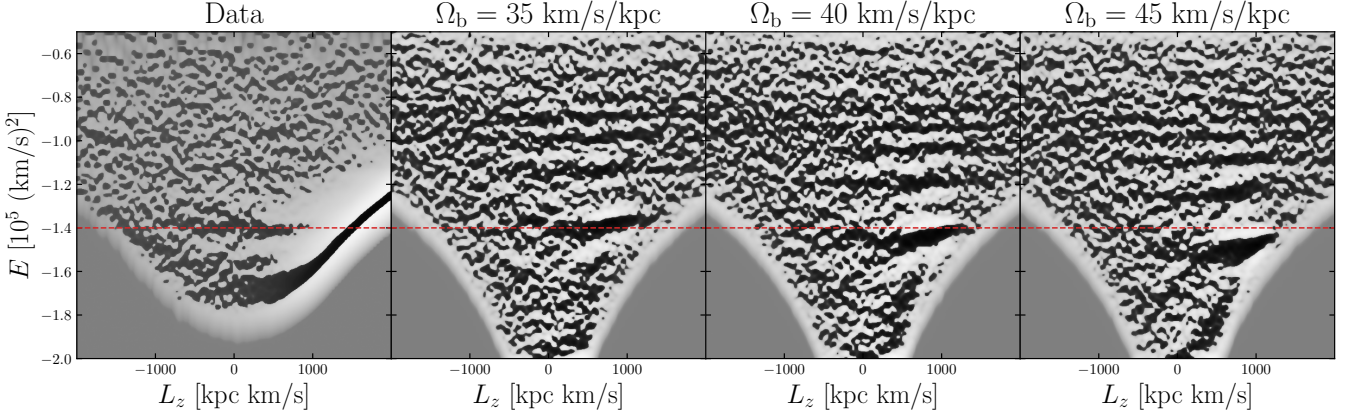


Figure 15. E - L_z distributions of the data (left-hand panel) and simulations with three different pattern speeds (right three panels). As in the bottom panel of Fig. 3, the data have been weighted and unsharp filtering has been applied to each distribution in energy. Black (white) pixels denote overdensities (underdensities). The red dashed line marks the approximate energy of the horizontal ridge in the data at $L_z > 0$. As the pattern speed is increased, the horizontal ridges in the simulations decrease in energy (and increase in frequency). The most prominent one (due to the corotation resonance) roughly aligns with the ridge in the data at a pattern speed of $\Omega_b \approx 35 - 40 \text{ km s}^{-1} \text{ kpc}^{-1}$.

$\text{km s}^{-1} \text{ kpc}^{-1}$ with the same background potential and initial distribution function. We calculate the energy E and angular momentum L_z of the particles, and apply unsharp masking to the E - L_z distributions similar to that used in Fig. 3. The filtered E - L_z distributions for the data and three simulations are shown in Fig. 15 with the approximate energies of the observed ridges marked by red dashed lines.

As the pattern speed Ω_b is increased, the frequencies of the resonances increase. This results in a decrease of the energies of the corresponding overdensities in E - L_z space. Of the three simulations, the closest match is at a pattern speed of $\Omega_b = 35 \text{ km s}^{-1} \text{ kpc}^{-1}$, at which the energy of the corotation ridge is $-1.4 \times 10^5 \text{ km}^2 \text{ s}^{-2}$. The $\Omega_b = 40 \text{ km s}^{-1} \text{ kpc}^{-1}$ model is also a reasonably good fit, while at $45 \text{ km s}^{-1} \text{ kpc}^{-1}$ the energy of the corotation ridge is too low to match the data.

We therefore conclude that pattern speeds in the range $35 - 40 \text{ km s}^{-1} \text{ kpc}^{-1}$ produce good matches between the energies of the observed and simulated ridges in E - L_z space. This is in agreement with most recent studies that constrain the pattern speed. For example, Chiba et al. (2021) and Binney (2020) found that $\Omega_b \approx 35.5$ and $36 \text{ km s}^{-1} \text{ kpc}^{-1}$ respectively were favoured, while Portail et al. (2017), Wang et al. (2013) and Sanders et al. (2019) preferred values in the range $39 - 41 \text{ km s}^{-1} \text{ kpc}^{-1}$.

5 CONCLUSIONS

Bars are important drivers of morphological changes in galaxies. The Milky Way is no exception. Its massive bar extends to around Galactocentric distances of $\approx 5 \text{ kpc}$ and contains $\approx 30 - 40$ per cent of the total stellar mass in the Galaxy. This hefty structure has long been known to drive evolution in the disc through its resonances. These are the locations where a combination of the stars' natural frequencies is equal to the forcing frequency or pattern speed of the bar. At the resonances, secular changes in the orbits occur, causing long term effects in the stellar populations.

Data from the *Gaia* satellite has reinvigorated the study of substructure in the disc. Many of the notches, ridges and ripples in phase space have been interpreted as the imprints of resonances with

the bar (e.g., Khoperskov et al. 2020; Trick et al. 2021; Trick 2022), though the effects of spirality driven by the bar are also possible (Hunt et al. 2018). The Hercules and Sirius streams in the solar neighbourhood were previously associated with the outer Lindblad resonance of the bar (Kalnajs 1991; Dehnen 1998). This requires the bar to have a high pattern speed. Nowadays, the corotation resonance of a slow bar with pattern speed $\Omega_b \approx 40 \text{ km s}^{-1} \text{ kpc}^{-1}$ is seen as the more likely explanation (e.g. Monari et al. 2019). There have also been hints that the bar may affect both streams (Hattori et al. 2016) and stellar populations in the halo (e.g., Moreno et al. 2015b; Myeong et al. 2018; Schuster et al. 2019).

In this paper, we have identified a distinctive feature in the phase space distribution of halo stars. It is a prominent ridge at energies $E \approx -1.4 \times 10^5 \text{ km}^2 \text{ s}^{-2}$ and with $L_z > 0$. This is apparent when data from the *Gaia* Data Release 3 (DR3) Radial Velocity Spectrometer (RVS) sample is plotted in energy versus angular momentum (E - L_z) space. It was also seen by Myeong et al. (2018), albeit with a much smaller dataset. Further ridges are also present before weighting, but they are likely artefacts caused by the selection function. The prominent ridge corresponds to a chevron-shaped overdensity in radial velocity versus radius (v_r - r) space previously reported by Belokurov et al. (2023). It resembles those produced by phase mixing the debris of a merged satellite galaxy (e.g. Fillmore & Goldreich 1984; Sanderson & Helmi 2013; Dong-Páez et al. 2022; Belokurov et al. 2023). However, the structure persists at both high and low metallicity ($[\text{Fe}/\text{H}] > -0.7$ and < -0.7), suggesting that the chevron is not composed of stars accreted from *Gaia* Sausage-Enceladus or elsewhere. It is natural to seek a dynamical solution for its provenance, as stars of all metallicities are affected.

To understand its origin, we run test particle simulations of a stellar halo population of particles under the influence of a rotating bar. After generating a steady-state distribution in an axisymmetric potential, we smoothly increase the bar strength over a period of 2 Gyr. The bar remains steady for the final 4 Gyrs of its life. The resultant distribution of stars in E - L_z and v_r - r space shows features similar to the data. Particles move from around $L_z \approx 0$ into ridges at $L_z > 0$, with both E and L_z increasing, so as to approximately conserve the Jacobi integral. When plotted in radial phase space, the ridges appear as chevrons. At the end of the simulation, the

azimuthal and radial frequencies Ω_ϕ and Ω_R are strongly clustered about certain values. These correspond to resonances with the bar, especially the corotation resonance and outer Lindblad resonance. It is the corotation resonance that is responsible for the most prominent ridge in E - L_z space. We plot the orbits of particles close to these resonances. Some are disc-like, but some are halo-like with large vertical excursions from the Galactic plane.

The bar spins up the inner stellar halo. We show this by calculating the spherically averaged median azimuthal velocity v_ϕ as a function of cylindrical radius R in our simulations. The average v_ϕ at $R \lesssim 10$ kpc is increased, so the simulated stellar halo gains a net spin. The observational data on the metal-poor star subsample from APOGEE shows qualitatively the same trend as the simulations, with the median v_ϕ decreasing from ≈ 70 to 10 km s^{-1} between Galactocentric radii R of 3 and 9 kpc. The effect of a bar spinning up a spheroidal distribution has been extensively studied in relation to the dark halo (e.g. Weinberg 1985; Athanassoula 2002) and the bulge (e.g. Saha et al. 2012, 2016). Dynamical friction acts on the bar, transferring its angular momentum to the halo and reducing the pattern speed (Hernquist & Weinberg 1992; Debattista & Sellwood 2000b). However, this process is not simple; Chiba & Schönrich (2022) showed that the dynamical friction can oscillate, resulting in the pattern speed oscillating while it decays. The efficiency of the angular momentum transfer depends on the mass of the spheroidal distribution, with less massive bulges being spun up more easily (Saha et al. 2016). We therefore note that while our test particle simulation provides an illustration of this effect, an N -body simulation with a live bar, disc and halo is required to quantify it and fully capture its complexity.

The distribution of the angular momentum becomes asymmetric. This asymmetry is more pronounced for stars with low J_z . As a result, a population of stars on seemingly disc-like orbits is forged from the initially non-rotating and smooth halo distribution. These orbits are similar to those previously reported for metal-poor, very metal-poor and extremely metal-poor stars in studies advocating a disc-like state for the high-redshift Galaxy (see e.g. Sestito et al. 2019; Di Matteo et al. 2020; Mardini et al. 2022). If following our results, the necessity for a pre-historic disc is removed, a different picture emerges. Before spinning up into a coherently rotating disc at metallicities $-1.5 < [\text{Fe}/\text{H}] < -1$, the early Milky Way was instead a kinematically hot and messy place in line with the analysis by Belokurov & Kravtsov (2022). This pre-disc Milky Way population, dubbed *Aurora*, is strongly centrally concentrated and thus lies predominantly within Solar radius and has a modest net spin (see Belokurov & Kravtsov 2022). Similar conclusions as to the state of the high-redshift Galaxy are reached in recent observational (Conroy et al. 2022; Rix et al. 2022; Myeong et al. 2022) and theoretical (Gurvich et al. 2023; Hopkins et al. 2023) studies.

We repeat our simulation with different bar pattern speeds in the range $35\text{--}45 \text{ km s}^{-1} \text{ kpc}^{-1}$. As the pattern speed of the bar is increased, the frequencies of the resonances increase. This decreases the energy of the horizontal ridges in E vs L_z space, as well as the radial extent of the corresponding chevron over-densities in v_r vs r space. We find that, with our choice of potential, a pattern speed of $\Omega_b \approx 35 - 40 \text{ km s}^{-1} \text{ kpc}^{-1}$ is required to match the energy of the most prominent ridge in E - L_z space. This is consistent with most recent estimates of the Milky Way bar's pattern speed, most of which are $35 - 41 \text{ km s}^{-1} \text{ kpc}^{-1}$ (e.g. Wang et al. 2013; Portail et al. 2017; Sanders et al. 2019; Binney 2020; Chiba & Schönrich 2021). While our results suggest that $35 \text{ km s}^{-1} \text{ kpc}^{-1}$ may be slightly favoured over $40 \text{ km s}^{-1} \text{ kpc}^{-1}$, a more detailed study is required to include consideration of uncertainties in the potential.

There are a number of avenues for further exploration. First, this

offers up a new tool to study the Galactic bar. Its formation epoch and its evolution will imprint themselves on the stellar halo as well as the disc. If the pattern speed of the bar is slowing because of dynamical friction exerted by the dark halo, this may induce detectable features in the ridges of the stellar halo populations. Secondly, the Lindblad and other resonances may also be the sites of depletions and enhancements in the action space of the stellar halo, though these have not yet been unambiguously associated with structures in the data. Thirdly, the bar may also create resonant features in the dark halo. This may be important if the substructures coincide with the solar neighbourhood, as this may enhance the signal expected in direct detection experiments in Earth-borne laboratories. We are actively pursuing these investigations and will report results in a future work.

ACKNOWLEDGEMENTS

We thank the anonymous referee for very helpful comments that have improved this manuscript. We are grateful to the Cambridge Streams group and Hans-Walter Rix for insightful discussions during this study. AMD and EYD thank the Science and Technology Facilities Council (STFC) for PhD studentships.

This work has made use of data from the European Space Agency (ESA) mission *Gaia* (<https://www.cosmos.esa.int/gaia>), processed by the *Gaia* Data Processing and Analysis Consortium (DPAC, <https://www.cosmos.esa.int/web/gaia/dpac/consortium>). Funding for the DPAC has been provided by national institutions, in particular the institutions participating in the *Gaia* Multilateral Agreement.

This research made use of Astropy,¹ a community-developed core Python package for Astronomy (Astropy Collaboration et al. 2013, 2018). This work was funded by UKRI grant 2604986. For the purpose of open access, the author has applied a Creative Commons Attribution (CC BY) licence to any Author Accepted Manuscript version arising.

DATA AVAILABILITY

This study uses publicly available *Gaia* data.

REFERENCES

- Abdurro'uf et al., 2022, *ApJS*, **259**, 35
- Arnold V. I., 1978, *Mathematical methods of classical mechanics*
- Astropy Collaboration et al., 2013, *A&A*, **558**, A33
- Astropy Collaboration et al., 2018, *AJ*, **156**, 123
- Athanassoula E., 2002, *ApJ*, **569**, L83
- Bailer-Jones C. A. L., Rybizki J., Fouesneau M., Demleitner M., Andrae R., 2021, *AJ*, **161**, 147
- Belokurov V., Kravtsov A., 2022, *MNRAS*, **514**, 689
- Belokurov V., Erkal D., Evans N. W., Koposov S. E., Deason A. J., 2018, *MNRAS*, **478**, 611
- Belokurov V., Vasiliev E., Deason A. J., Koposov S. E., Fattahi A., Dillamore A. M., Davies E. Y., Grand R. J. J., 2023, *MNRAS*, **518**, 6200
- Benjamin R. A., et al., 2005, *ApJ*, **630**, L149
- Binney J., 2012, *MNRAS*, **426**, 1324
- Binney J., 2020, *MNRAS*, **495**, 895
- Binney J., Tremaine S., 2008, *Galactic Dynamics: Second Edition*
- Binney J., Gerhard O. E., Stark A. A., Bally J., Uchida K. I., 1991, *MNRAS*, **252**, 210

¹ <http://www.astropy.org>

- Bissantz N., Englmaier P., Gerhard O., 2003, *MNRAS*, **340**, 949
- Bland-Hawthorn J., Gerhard O., 2016, *ARA&A*, **54**, 529
- Blitz L., Spergel D. N., 1991, *ApJ*, **379**, 631
- Bovy J., 2015, *ApJS*, **216**, 29
- Cabrera-Lavers A., Hammersley P. L., González-Fernández C., López-Corredoira M., Garzón F., Mahoney T. J., 2007, *A&A*, **465**, 825
- Cabrera-Lavers A., González-Fernández C., Garzón F., Hammersley P. L., López-Corredoira M., 2008, *A&A*, **491**, 781
- Ceverino D., Klypin A., 2007, *MNRAS*, **379**, 1155
- Chiba R., Schönrich R., 2021, *MNRAS*, **505**, 2412
- Chiba R., Schönrich R., 2022, *MNRAS*, **513**, 768
- Chiba R., Friske J. K. S., Schönrich R., 2021, *MNRAS*, **500**, 4710
- Churchwell E., et al., 2009, *PASP*, **121**, 213
- Collett J. L., Dutta S. N., Evans N. W., 1997, *MNRAS*, **285**, 49
- Collier A., Shlosman I., Heller C., 2019, *MNRAS*, **488**, 5788
- Conroy C., et al., 2022, arXiv e-prints, p. arXiv:2204.02989
- Contopoulos G., 1980, *A&A*, **81**, 198
- Davies E. Y., Vasiliev E., Belokurov V., Evans N. W., Dillamore A. M., 2023a, *MNRAS*, **519**, 530
- Davies E. Y., Dillamore A. M., Vasiliev E., Belokurov V., 2023b, *MNRAS*, **521**, L24
- Deason A. J., Belokurov V., Evans N. W., 2011, *MNRAS*, **416**, 2903
- Debattista V. P., Sellwood J. A., 1998, *ApJ*, **493**, L5
- Debattista V. P., Sellwood J. A., 2000a, *ApJ*, **543**, 704
- Debattista V. P., Sellwood J. A., 2000b, *ApJ*, **543**, 704
- Dehnen W., 1998, *AJ*, **115**, 2384
- Dehnen W., 2000, *AJ*, **119**, 800
- Di Matteo P., Spite M., Haywood M., Bonifacio P., Gómez A., Spite F., Caffau E., 2020, *A&A*, **636**, A115
- Dong-Páez C. A., Vasiliev E., Evans N. W., 2022, *MNRAS*, **510**, 230
- Faccioli L., Smith M. C., Yuan H. B., Zhang H. H., Liu X. W., Zhao H. B., Yao J. S., 2014, *ApJ*, **788**, 105
- Feuillet D. K., Sahlholdt C. L., Feltzing S., Casagrande L., 2021, *MNRAS*, **508**, 1489
- Fillmore J. A., Goldreich P., 1984, *ApJ*, **281**, 1
- Fragkoudi F., et al., 2019, *MNRAS*, **488**, 3324
- Fux R., 1999, *A&A*, **345**, 787
- Gaia Collaboration et al., 2016, *A&A*, **595**, A1
- Gaia Collaboration et al., 2023a, *A&A*, **674**, A1
- Gaia Collaboration et al., 2023b, *A&A*, **674**, A37
- González-Fernández C., López-Corredoira M., Amôres E. B., Minniti D., Lucas P., Toledo I., 2012, *A&A*, **546**, A107
- Gurvich A. B., et al., 2023, *MNRAS*, **519**, 2598
- Hammersley P. L., Garzon F., Mahoney T., Calbet X., 1994, *MNRAS*, **269**, 753
- Hammersley P. L., Garzón F., Mahoney T. J., López-Corredoira M., Torres M. A. P., 2000, *MNRAS*, **317**, L45
- Hattori K., Erkal D., Sanders J. L., 2016, *MNRAS*, **460**, 497
- Helmi A., Babusiaux C., Koppelman H. H., Massari D., Veljanoski J., Brown A. G. A., 2018, *Nature*, **563**, 85
- Hernquist L., Weinberg M. D., 1992, *ApJ*, **400**, 80
- Hopkins P. F., et al., 2023, *MNRAS*,
- Hunt J. A. S., Hong J., Bovy J., Kawata D., Grand R. J. J., 2018, *MNRAS*, **481**, 3794
- Kalnajs A. J., 1991, in Sundelius B., ed., *Dynamics of Disc Galaxies*. p. 323
- Katz D., et al., 2023, *A&A*, **674**, A5
- Khoperskov S., Gerhard O., Di Matteo P., Haywood M., Katz D., Khrapov S., Khoperskov A., Arnaboldi M., 2020, *A&A*, **634**, L8
- Kruijssen J. M. D., et al., 2020, *MNRAS*, **498**, 2472
- Li Z., Shen J., Gerhard O., Clarke J. P., 2022, *ApJ*, **925**, 71
- Lucey M., Pearson S., Hunt J. A. S., Hawkins K., Ness M., Petersen M. S., Price-Whelan A. M., Weinberg M. D., 2023, *MNRAS*, **520**, 4779
- Lynden-Bell D., 1973, in Contopoulos G., Henon M., Lynden-Bell D., eds, *Saas-Fee Advanced Course 3: Dynamical Structure and Evolution of Stellar Systems*. p. 91
- Lynden-Bell D., Kalnajs A. J., 1972, *MNRAS*, **157**, 1
- Majewski S. R., et al., 2017, *AJ*, **154**, 94
- Mardini M. K., Frebel A., Chiti A., Meiron Y., Brauer K. V., Ou X., 2022, *ApJ*, **936**, 78
- Martinez-Valpuesta I., Gerhard O., 2011, *ApJ*, **734**, L20
- Molloy M., Smith M. C., Shen J., Evans N. W., 2015, *ApJ*, **804**, 80
- Monari G., Famaey B., Siebert A., Grand R. J. J., Kawata D., Boily C., 2016, *MNRAS*, **461**, 3835
- Monari G., Famaey B., Siebert A., Wegg C., Gerhard O., 2019, *A&A*, **626**, A41
- Moreno E., Pichardo B., Schuster W. J., 2015a, *MNRAS*, **451**, 705
- Moreno E., Pichardo B., Schuster W. J., 2015b, *MNRAS*, **451**, 705
- Myeong G. C., Evans N. W., Belokurov V., Sanders J. L., Koposov S. E., 2018, *ApJ*, **856**, L26
- Myeong G. C., Belokurov V., Aguado D. S., Evans N. W., Caldwell N., Bradley J., 2022, *ApJ*, **938**, 21
- Naidu R. P., Conroy C., Bonaca A., Johnson B. D., Ting Y.-S., Caldwell N., Zaritsky D., Cargile P. A., 2020, *ApJ*, **901**, 48
- Pila-Diez B., de Jong J. T. A., Kuijken K., van der Burg R. F. J., Hoekstra H., 2015, *A&A*, **579**, A38
- Portail M., Gerhard O., Wegg C., Ness M., 2017, *MNRAS*, **465**, 1621
- Posti L., Binney J., Nipoti C., Ciotti L., 2015, *MNRAS*, **447**, 3060
- Rix H.-W., et al., 2022, *ApJ*, **941**, 45
- Rosas-Guevara Y., et al., 2022, *MNRAS*, **512**, 5339
- Saha K., Martinez-Valpuesta I., Gerhard O., 2012, *MNRAS*, **421**, 333
- Saha K., Gerhard O., Martinez-Valpuesta I., 2016, *A&A*, **588**, A42
- Sanders J. L., Binney J., 2016, *MNRAS*, **457**, 2107
- Sanders J. L., Smith L., Evans N. W., 2019, *MNRAS*, **488**, 4552
- Sanderson R. E., Helmi A., 2013, *MNRAS*, **435**, 378
- Schuster W. J., Moreno E., Fernández-Trincado J. G., 2019, in McQuinn K. B. W., Stierwalt S., eds, *Proc. IAU Symp. Vol. 344, Dwarf Galaxies: From the Deep Universe to the Present*. pp 134–138 (arXiv:1811.09827), doi:10.1017/S174392131800683X
- Sestito F., et al., 2019, *MNRAS*, **484**, 2166
- Shu F., 1991, *Physics of Astrophysics, Vol. II: Gas Dynamics*
- Silva J. S., Schuster W. J., Contreras M. E., 2012, *Rev. Mex. Astron. Astrofis.*, **48**, 109
- Simion I. T., Belokurov V., Irwin M., Koposov S. E., Gonzalez-Fernandez C., Robin A. C., Shen J., Li Z. Y., 2017, *MNRAS*, **471**, 4323
- Sormani M. C., Binney J., Magorrian J., 2015, *MNRAS*, **454**, 1818
- Stanek K. Z., Mateo M., Udalski A., Szymanski M., Kaluzny J., Kubiak M., 1994, *ApJ*, **429**, L73
- Stanek K. Z., Udalski A., Szymański M., KaŁuŻny J., Kubiak Z. M., Mateo M., Krzemiński W., 1997, *ApJ*, **477**, 163
- Tremaine S., Weinberg M. D., 1984, *ApJ*, **282**, L5
- Trick W. H., 2022, *MNRAS*, **509**, 844
- Trick W. H., Fragkoudi F., Hunt J. A. S., Mackereth J. T., White S. D. M., 2021, *MNRAS*, **500**, 2645
- Vasiliev E., 2019, *MNRAS*, **482**, 1525
- Wang Y., Mao S., Long R. J., Shen J., 2013, *MNRAS*, **435**, 3437
- Watkins L. L., et al., 2009, *MNRAS*, **398**, 1757
- Wegg C., Gerhard O., Portail M., 2015, *MNRAS*, **450**, 4050
- Weiland J. L., et al., 1994, *ApJ*, **425**, L81
- Weinberg M. D., 1985, *MNRAS*, **213**, 451
- Weinberg M. D., Katz N., 2002, *ApJ*, **580**, 627
- Wheeler A., Abril-Cabezas I., Trick W. H., Fragkoudi F., Ness M., 2022, *ApJ*, **935**, 28
- Whitlock P., 1992, in Warner B., ed., *Astronomical Society of the Pacific Conference Series Vol. 30, Variable Stars and Galaxies, in honor of M. W. Feast on his retirement*. p. 11
- Williams A. A., Evans N. W., 2015, *MNRAS*, **448**, 1360
- de Vaucouleurs G., 1964, in Kerr F. J., ed., *Proc. IAU Symp. Vol. 20, The Galaxy and the Magellanic Clouds*. p. 195
- de Zeeuw T., 1985, *MNRAS*, **216**, 273

This paper has been typeset from a \LaTeX file prepared by the author.